catalysts

MDPI

Article

Wastewater Purification and All-Solid Z-Scheme Heterojunction ZnO-C/MnO_2 Preparation: Properties and Mechanism

Lei Zhao [1], Tingting Yu [1,2,*], Bing Yang [1], Huilin Guo [1], Lifen Liu [3], Jinlong Zhang [4], Changfei Gao [5], Tao Yang [1], Mingyan Wang [1] and Yu Zhang [6]

1 School of Environmental and Chemical Engineering, Jiangsu Ocean University, Lianyungang 222005, China
2 Marine Resources Development Institute of Jiangsu, Jiangsu Ocean University, Lianyungang 222005, China
3 Key Laboratory of Industrial Ecology and Environmental Engineering, MOE, School of Environmental Science and Technology, Dalian University of Technology, Dalian 116024, China
4 Key Laboratory for Advanced Materials, Shanghai Engineering Research Center for Multi-media Environmental Catalysis and Resource Utilization, Joint International Research Laboratory of Precision Chemistry and Molecular Engineering, Feringa Nobel Prize Scientist Joint Research Center, School of Chemistry and Molecular Engineering, East China University of Science & Technology, Shanghai 200237, China
5 School of Environmental and Material Engineering, Yantai University, Yantai 264005, China
6 Lianyungang Gaopin Renewable Resources Co., Ltd., Lianyungang 222005, China
* Correspondence: ting@jou.edu.cn; Tel.: +86-15189022543

Abstract: Unlike many studies on the preparation of Z-scheme heterojunctions by doping precious metals, in this paper we first prepared a core-shell material obtained by C doping in ZnO and then composite with MnO_2 to form a heterojunction; that is, a low-cost and highly catalytic ternary composite catalyst was prepared by a simple hydrothermal reaction. Meanwhile, a large amount of experimental data have enabled the heterostructure type as well as the mechanism of photocatalytic performance to be fully demonstrated. It is proven that C as an intermediate medium achieves electron transport while making up the deficiency of ZnO, and constitutes an all-solid state Z-scheme heterojunction, which enables the rapid transfer of photogenerated electron pairs and visible light irradiation to the stream to improve the photocatalytic performance of the composite photocatalyst. In terms of examination of degradation performance, this catalyst showed a high photodegradation rate of tetracycline hydrochloride (TC) of 92.6% within 60 min, and the surface ZnO-C/MnO_2 catalysts also showed good degradation effect on practical petrochemical wastewater in CODcr degradation experiments.

Keywords: ZnO-C/MnO_2; Z-scheme heterojunction; wastewater purification; mechanism exploring

check for updates

Citation: Zhao, L.; Yu, T.; Yang, B.; Guo, H.; Liu, L.; Zhang, J.; Gao, C.; Yang, T.; Wang, M.; Zhang, Y. Wastewater Purification and All-Solid Z-Scheme Heterojunction ZnO-C/MnO_2 Preparation: Properties and Mechanism. *Catalysts* **2022**, *12*, 1250. https://doi.org/10.3390/catal12101250

Academic Editors: Jiangkun Du, Lie Yang and Chengdu Qi

Received: 16 September 2022
Accepted: 13 October 2022
Published: 16 October 2022

1. Introduction

Lots of research indicates that more and more antibiotics frequently found in the surface water and urban sewage treatment have become new water pollutants with harmful ecological effects [1–4]. In the past few decades, as serious environmental and energy-related problems have increased around the world, heterogeneous photocatalysis based on semiconductors been seen as one of the most promising solutions to these crises [5–8]. At present, photocatalysis has been widely applied to the field of environmental governance. The key point of efficient photocatalysis is the design and preparation of highly active semiconductors, in which ZnO has the advantages of suitable band gap, non-toxicity, environmental sustainability, low cost, and abundant resources. Nevertheless, there are limitations in practical application owing to its shortcomings, such as the fast recombination speed of light-induced electron hole pairs and the optical instability in aqueous solution [9,10].

Experiments show that the above defects can be effectively surmounted by modifying the surface of ZnO [11,12], such as the separation and light absorption characteristics of ZnO can be adjusted by internal defects and external impurities [13–15]. The reason why non-metallic doping is considered the most effective strategy is that doping can not

only increase the electron density of Fermi level and introduce vacancy states in the band gap [7,16,17], but also change the effective mass of charge carriers and have an important impact on charge transfer, transfer, and separation [6,18]. In addition to doping nonmetals to improve the catalytic efficiency, the semiconductor composite is also a common method to study the ZnO-TiO_2 and ZnO-SnO_2 semiconductor composite systems; a series of nano-TiO_2/ZnO composite mesoporous materials were synthesized by homogeneous precipitation method [19].

In addition, manganese dioxide, a natural resource-rich, low-cost material, is environmentally friendly and has a high theoretical specific capacitance (1370 F/g), it is widely used in the capacitor, electrochemistry, photocatalysis, biosensor, and other fields [20–22]. There are mainly four crystallographic forms of MnO_2, namely α-, β-, γ-, and δ-MnO_2, which has a unique tunnel structure or interlayer, in which δ-MnO_2 has the best performance [23]. The principle of MnO_2 photocatalysis is the use of light to stimulate MnO_2 semiconductor through the photoelectrons and holes generated by the oxidation-reduction reaction, for the photocatalytic degradation of organic compounds, most of the MnO_2 nanomaterials also have some defects, such as a single type of dye degradation, low degradation efficiency, or adding oxidant (such as H_2O_2) to promote photocatalytic reaction [24]. Although the utilization of visible light is high, the band gap is too narrow and the recombination speed of photocarriers is very fast. Therefore, the combination of manganese dioxide and band-gap semiconductor photocatalytic materials can not only improve the absorption of visible light, but also rapidly separate photoelectrons and holes by constructing heterojunctions to improve the catalytic activity [25–27]. In the discussion of the formation and configuration of the heterojunction, the ZnO-C/MnO_2 heterojunction is more Z-scheme, especially in an all-solid-state. For now, many all-solid-state Z-scheme semiconductor photocatalysis systems have been reported and have shown good performance in various photocatalytic applications, for example, CdS/Au/Bi_2MoO_6 [28], α-Fe_2O_3/CdS/g-C_3N_4 [29], g-C_3N_4/ZnO/$Bi_4O_5Br_2$ [30], Ta_3N_5/Bi/$CaTaO_2N$ [31], and BiOCl-Au-CdS [32]. Table 1 shows a comparison of catalytic degradation related to ZnO and MnO_2, including comparison of heterojunction type, pollutant type, and degradation effect.

Table 1. The comparison of catalytic degradation related to ZnO and MnO_2.

Catalyst Composition	Type	Name of Pollution	Degradation Efficiency	References
SDS/ZnO	Type-II	TC	49%	[33]
α-MnO_2		TC	51.55%	[34]
C/ZnO/BiOI	Type-II	carbaryl	62.9%	[35]
δ-MnO_2/h-MoO_3	Type-II	MO	80.55%	[36]
$ZnFe_2O_4$/C/MnO_2	Type-II	MO	91%	[37]
Bi_2MoO_6/$ZnSnO_3$/ZnO	Type-Z	TC	90%	[38]
Fe_3O_4/C/MnO_2/C_3N_4	Type-Z	MO	94.11%	[39]
ZnO/g-C_3N_4	Type-Z	MB	95.4%	[40]

The catalyst synthesized in this paper is different from the traditional Z-scheme semiconductor. C is used as the intermediate medium as the electron transmission channel, rather than the three-way catalyst composed of precious metals such as the intermediate, which reduces the cost to a certain extent. At the same time, with the support of many characterization experiments, it can be proved that the C-link extends the light response range of the catalyst through the plasma resonance effect. Through multiple control tests, it is proved that ZnO-C/MnO_2, as a new semiconductor catalyst of Z-scheme, has a high degradation effect, and has a certain interpretation effect on actual wastewater.

2. Results and Discussion

2.1. Representational Analysis

Figure 1 is the X-ray diffraction (XRD) pattern of ZnO-C nanospheres, MnO_2 nanowires, and ZnO-C/MnO_2 heterojunction. Determine the crystal form of powder material according to Joint Committee on Powder Diffraction Standards (JCPDS). It can be seen that ZnO-C has three main characteristic diffraction peaks at 31.8°, 34.4°, and 36.3°, which correspond to the (100), (002), and (101) crystal plane, respectively. MnO_2 at 2θ = 28°, 37°, 42°, 56°, and 72° have obvious characteristic peaks, and the diffraction peaks are sharp, consistent with the standard card (JCPDS 81-2261) β-MnO_2. The intensity of MnO_2 peak in the complex decreases, which may be due to the strong characteristic peak of ZnO, which masks the peak of MnO_2 and leads to the weakening of MnO_2 diffraction intensity [41]. XRD patterns indicate that we successfully synthesized ZnO-C/MnO_2 composites with relatively good crystallinity.

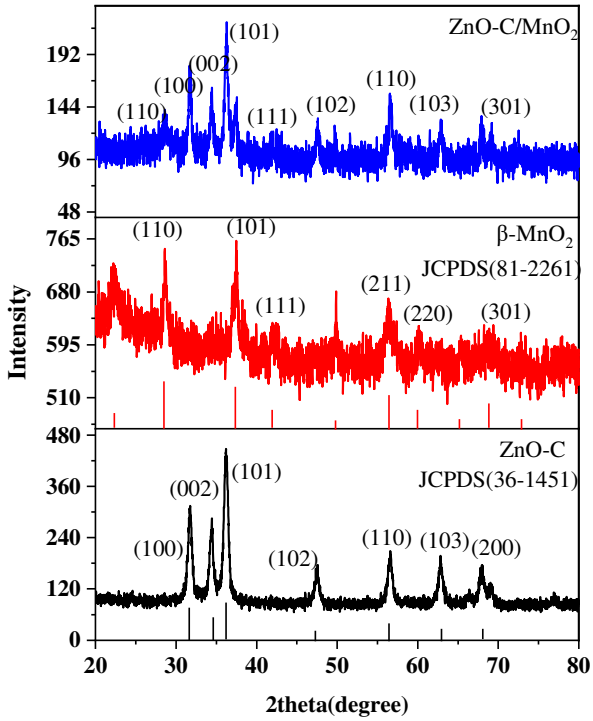

Figure 1. XRD patterns of ZnO-C, MnO_2, and ZnO-C/MnO_2.

The ZnO-C nanospheres, MnO_2 nanowires, and ZnO-C/MnO_2 composites are characterized by high-power scanning electron microscopy (SEM) and transmission electron microscope (TEM) in Figure 2. The ZnO shown in Figure 2a is spherical. There is a certain gap between the nano-spheres, which is conducive to the insertion and adhesion of the MnO_2 nanowires. Figure 3b shows a large number of MnO_2 nanowires interwoven together, and lines have many gaps, facilitating the ZnO-C connection. Figure 2c clearly shows many MnO_2 nanowires attached to ZnO-C nanospheres, the original smooth nanospheres become rough, indicating that ZnO-C provides a good adhesion point for MnO_2. In Figure 2d, the lattice spacing between the inner and outer sides is 0.259 nm and 0.304 nm, respectively. The lattice spacing between the inner and outer sides is different. Figure 2e shows that the lattice spacing of MnO_2 is about 0.218 nm. Figure 2f contains two kinds of lattice spacing, and the ZnO-C nanospheres are connected with the MnO_2 nanowires. This indicates that the composite is successful, combined with the energy dispersive spectroscopy (EDS) diagram of the composite in Figure 3. It can be seen that the elements contained are completely and evenly distributed.

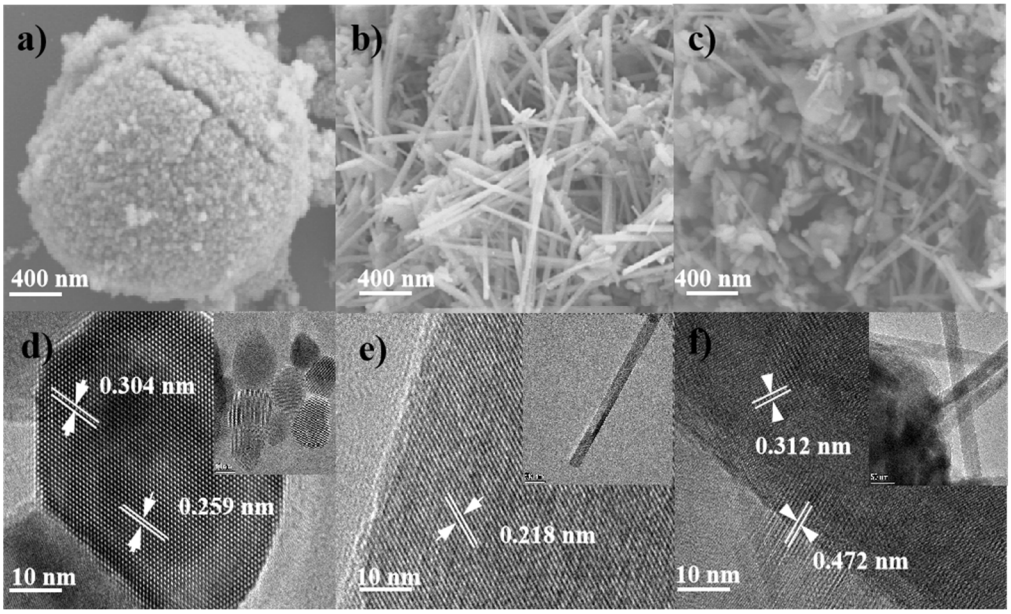

Figure 2. (**a**), EDS layered image of ZnO-C/MnO_2 (**b**), Element distribution image of C, O, Zn, Mn (**c**–**f**).

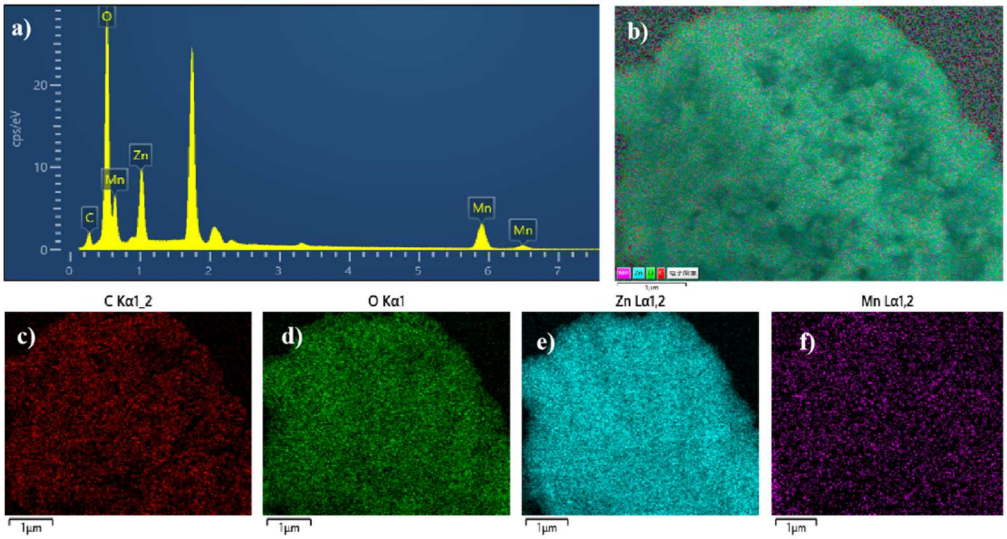

Figure 3. Total spectrum of ZnO-C/MnO_2 distribution map (**a**), EDS layered image of ZnO-C/MnO_2 (**b**), Element distribution image of C, O, Zn, Mn (**c**–**f**).

Figure 4 shows the ultraviolet visible diffuse reflectance spectroscopy (UV-vis) (a,b) and Mott-Schottky curves (c,d) of ZnO-C nanospheres, MnO_2 nanowires, and their composites. As can be seen from Figure 4a, ZnO-C has strong light absorption ability before 380 nm, MnO_2 has strong and stable light absorption strength, and ZnO-C/MnO_2 composite has strong light absorption ability before 450 nm. The energy gap of the photocatalyst is calculated by the following formula (Equation (1)) [42]:

$$Ah\nu = A(h\nu - Eg)n/2 \quad (1)$$

where α, H, ν, Eg, and A represent the absorption coefficient, optical efficiency, Planck constant, band-gap energy, and proportional constant, respectively. The curve of Figure 4b is formed through the above formula, which can be obtained because the band gap of ZnO-C is 3.06 eV, MnO_2 is 1.38 eV, and ZnO-C/MnO_2 is 2.7 eV. It can be found that C doping makes the band gap of ZnO wider, and the ternary composites have successfully widened the band gap. From the slope of the straight line in Figure 4c, it can be concluded

that ZnO-C and MnO_2 are p-type semiconductors [43], however, as a conventional n-type semiconductor [44], ZnO is shown to be p-type because the semiconductor is modified by a large number of impurities, and it is proved from the side that C is successfully doped in ZnO nanospheres. According to the intersection of tangent and x-axis, the flat band potential is 0.73 eV and −0.31 eV, respectively. Figure 4d is the M-S curve of the composite, showing an inverted V shape. Again, ZnO-C nanospheres and MnO_2 nanowires are successfully compounded together.

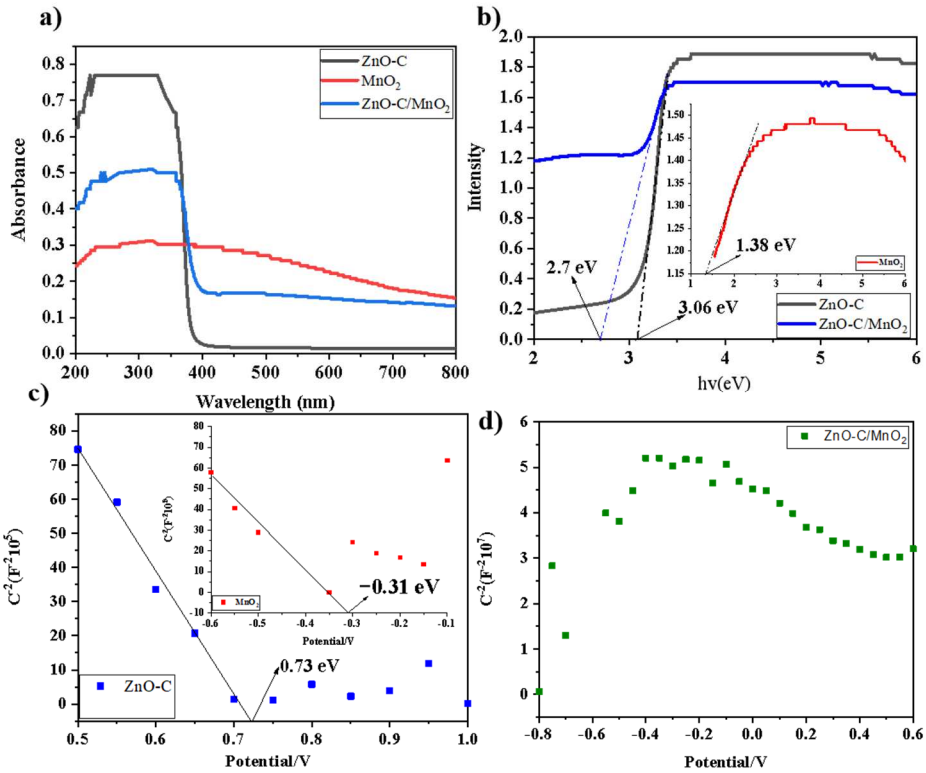

Figure 4. UV-vis spectra of ZnO-C nanospheres (**a**), MnO_2 nanowires and ZnO-C/MnO_2 heterojunction (**b**) and M-S of ZnO-C nanospheres, MnO_2 nanowires (**c**) and ZnO-C/MnO_2 (**d**).

To further prove the success of the ZnO-C/MnO_2 composite, the ZnO-C nanospheres, MnO_2 nanowires, and ZnO-C/MnO_2 composites were analyzed by X-ray photoelectron spectroscopy (XPS). Figure 5 shows the full XPS spectra and the narrow spectra of Zn 2p, Mn 2p, O 1s, and C 1s orbitals for the three materials. As can be seen from Figure 5a, the main elements of ZnO-C/MnO_2 nanocomposites are C, O, Zn, and Mn. From the high-resolution diagram d of C 1 s, it can be seen that ZnO-C is in the C 1s peak at 283.98 eV, MnO_2 is in the C 1s peak at 286.4 eV, and ZnO-C/MnO_2 is in the C 1s peak at 286.3 eV. Comparing the positions of the composite peaks, it can be seen that the C 1s orbitals in ZnO-C have electrons, loss of electrons in C 1s orbitals in MnO_2. It can be seen from the high-resolution diagram e of O 1s that ZnO-C is in the O 1s peak at 530.08 eV, 530.68 eV and 531.88 eV, MnO_2 is in the O 1s peak at 529.58 eV, 530.08 eV, 531.58 eV, and ZnO-C/MnO_2 is in the O_2^- [45] at 529.58 eV, 531.18 eV, and 532.28 eV. Figure 5b is a high resolution XPS map of Zn 2p. The binding energies of ZnO-C at 1021.28 eV and 1044.58 eV are attributed to Zn 2p3/2 and Zn 2p1/2, respectively. This indicates that Zn exists mainly as Zn^{2+} in the ZnO-C/MnO_2 heterostructure, Zn 2p3/2 and Zn 2p1/2 have a difference of 23.3 eV, which is consistent with the energy splitting of ZnO [46]. Figure 5c is a high resolution XPS map of Mn2p. The binding energies at 642.4 eV and 654 eV are attributed to Mn 2p3/2 and Mn 2p1/2, respectively. It is further proved that Mn in ZnO-C/MnO_2 is in the +4 Valence State, by comparing the peak shift of the composites, we can see that Zn loses an electron in 2p

orbit and Mn obtains electron in 2p orbit, which shows that ZnO-C and MnO_2 have been successfully combined, and C is used as the intermediate to realize the electron transfer.

Generally speaking, the thermodynamics of the band position of the sample determines the formation and consumption of photogenerated carriers. The positions of the conduction band (E_{CB}) and valence band (E_{VB}) are estimated by empirical formulas (Equations (2) and (3)) [47]:

$$E_{VB} = \chi - Ee + 0.5\ Eg\ (Ee = 4.5\ eV) \quad (2)$$

$$E_{CB} = E_{VB} - Eg \quad (3)$$

where χ is the geometric mean of the absolute electronegativity of the constituent atoms; for ZnO-C and MnO_2, χ is 5.75 eV, and 5.96 eV, respectively. Ee is a constant (approximately 4.5 eV) corresponding to the energy of free electrons on the hydrogen scale, Eg is the band-gap energy obtained by UV-vis spectra. Therefore, E_{CB} and E_{VB} are −0.08 and 2.98 (eV vs. NHE) for ZnO-C, and 0.77 and 2.15 (eV vs. NHE) for MnO_2.

However, in order to determine the energy band position of semiconductors in depth, valence band XPS spectroscopy was carried out. As shown in Figure 5f, the $E_{VB\text{-}XPS}$ of ZnO-C and MnO_2 are 2.39 and 0.52 eV. Owing to the existence of the contact potential difference, the VB potential should be revised by the following formula (Equation (4)) [48]:

$$E_{VB\text{-}NHE} = \varphi + E_{VB}\text{-xps} - 4.44 \quad (4)$$

where $E_{VB\text{-}NHE}$ represents the VB potential (eV vs. NHE), the φ is the work function of ZnO (4.82 eV) and MnO_2 (4.19 eV) [49,50]. Therefore, the E_{VB} of ZnO-C and MnO_2 are 2.77 V and 0.27 (eV vs. NHE), respectively. The E_{CB} of ZnO-C and MnO_2 are −0.29 and −1.1 (eV vs. NHE), respectively.

The photoluminescence (PL) intensity of a semiconductor can be determined by the recombination of photoinduced carriers. Generally, higher PL intensity means faster recombination of photoelectrons and holes [19]; separation of photocarriers before and after ZnO-C and MnO_2 nanowire recombination. Figure 6a shows the PL spectra of ZnO-C nanospheres and MnO_2 nanowires and ZnO-C/MnO_2 composites at 370 nm excitation light source. The emission peak at 522 nm is attributed to the single ionized oxygen vacancy. Compared with single ZnO-C and MnO_2, the luminescent intensity of ZnO-C/MnO_2 composites decreased, which indicates that heterostructure can effectively decrease the recombination efficiency of photoelectron-hole pairs, which would be beneficial to the enhancement of photocatalytic activity. Figure 6b is the photocurrent response diagram of ZnO-C, MnO_2, and ZnO-C/MnO_2. It is obvious that the photocurrent intensity of ZnO-C/MnO_2 composites is higher than that of single ZnO-C and MnO_2. The higher the photocurrent intensity is, the higher the efficiency of hole-electron pair separation is. Figure 6c is the EIS of ZnO-C nanospheres [51], MnO_2 nanowires, and composite materials. The arc radius of ZnO-C/MnO_2 is smaller than that of single ZnO-C and MnO_2, because the relative size of the arc on the Nyquist diagram corresponds to the size of the charge transfer resistance and the separation efficiency of the photoelectron-hole pair, the separation efficiency of ZnO-C/MnO_2 is better than that of the single photocatalyst [52].

2.2. Photocatalytic Performances

2.2.1. Degradation of Antibiotic Wastewater Simulated by TC

The degradation rate of TC in antibiotic wastewater by adding the same catalyst was studied under the same light intensity. The influence of different light conditions on the degradation rate of pollutants was determined with a spectrophotometer and compared with the proportion of catalysts with the highest catalytic efficiency. The results of Figure 7a show that the ratio of ZnO-C to MnO_2 is 1:1, and the degradation rate is 92.6%. The ZnO-C/MnO_2 material has been found to have high degradation efficiency and dependence after a lot of experiments, and it has a better degradation effect than the ternary or binary composite materials related to ZnO in other research [53].

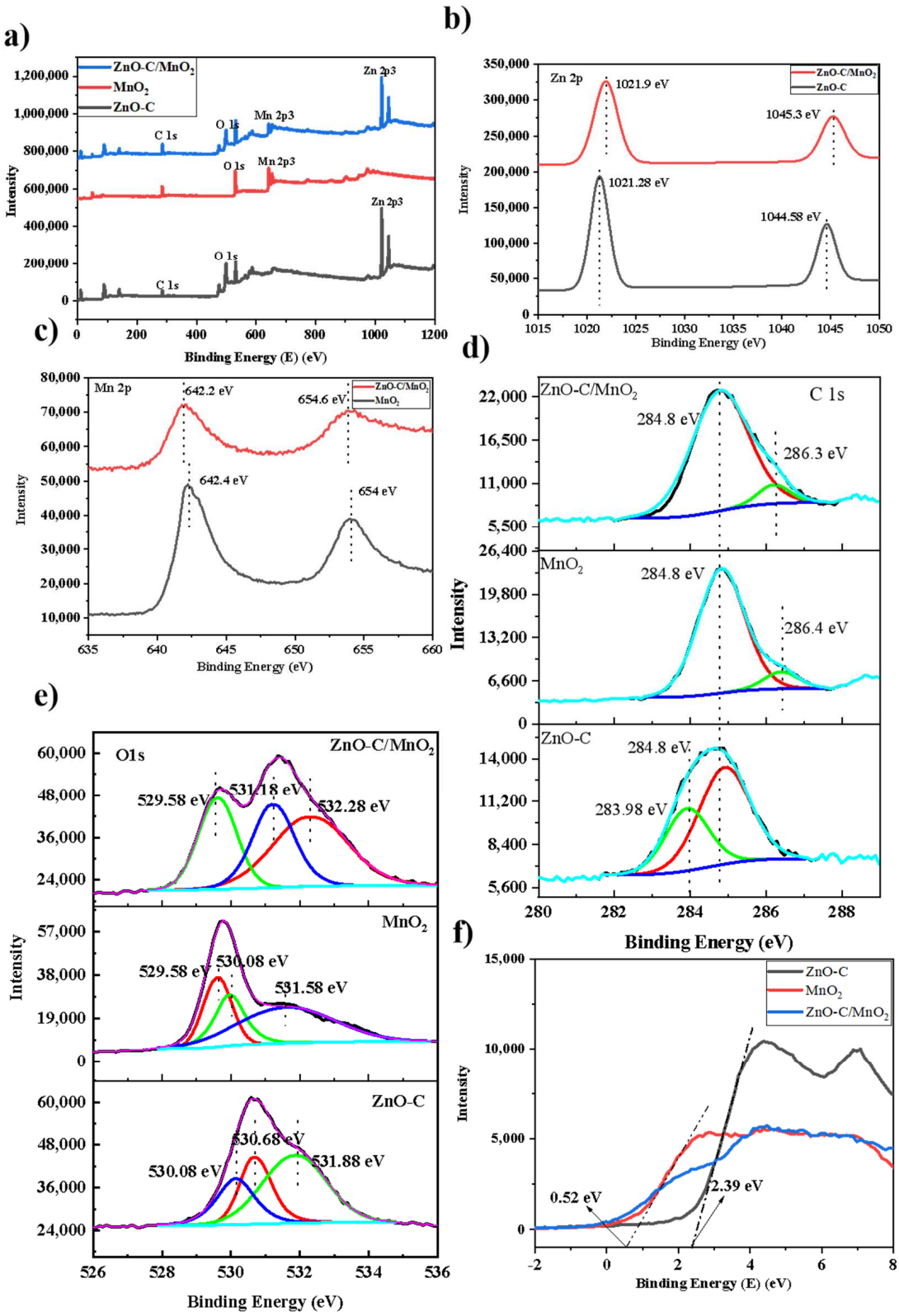

Figure 5. XPS spectra of survey spectra (**a**), Zn2p spectra (**b**), Mn2p spectra (**c**), C 1s spectra (**d**), O 1s spectra (**e**), VB-XPS of ZnO-C/MnO_2 (**f**).

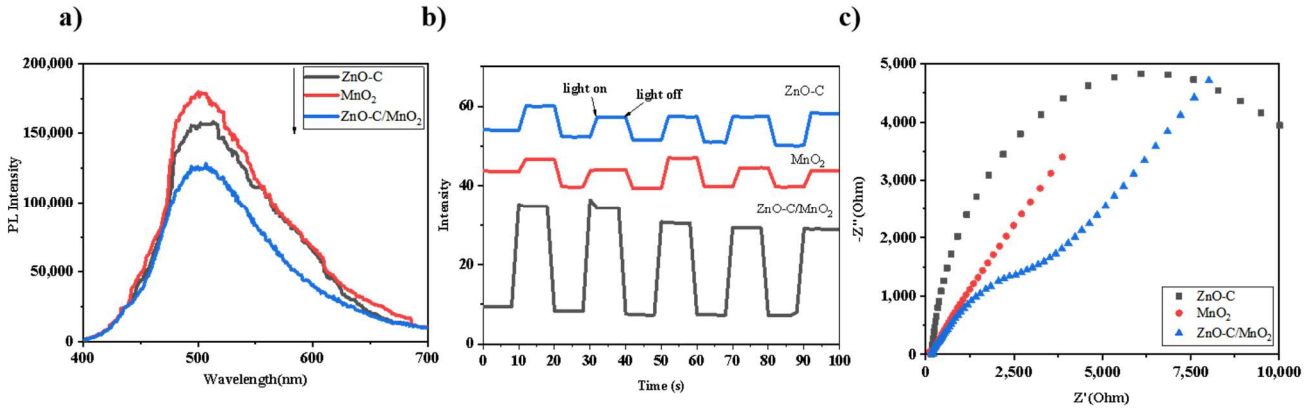

Figure 6. PL spectra of ZnO-C, MnO_2, and ZnO-C/MnO_2 under 370 nm excitation (**a**); transient photocurrent responses of ZnO-C, MnO_2, and ZnO-C/MnO_2 under xenon lamp irradiation (**b**); electrochemical impedance spectroscopy of ZnO-C, MnO_2, and ZnO-C/MnO_2 (**c**).

Figure 7b shows the absorbance analysis of the catalyst at the optimum ratio of 1:1. At the wavelength of 356 nm, it can be seen that the UV spectrophotometry of TC decreases with time, and finally tends to a straight line. The unique deconstructed catalyst is an excellent candidate for high-performance photocatalysts. Studies have shown that nanocrystalline subunits provide high specific surface area and porous structure, and have a variety of active photocatalysis sites [54].

Figure 7c,d reflect the photocatalytic activity of the composite catalyst under different catalyst dosage and pollutant concentrations. Aeration plays an important role in photocatalysis, which promotes the full contact between catalyst and pollutants. When the amount of catalyst is 20 mg/L, the catalytic effect is the best. With the increase in catalyst dosage, the improvement of TC degradation efficiency may be due to the increase in the number of active sites and the more effective interaction with TC. Under the irradiation of simulated sunlight, the photocatalyst is positively correlated with the rate of free radical production, which leads to an increase in the rate of photocatalytic degradation of TC. However, a high catalyst dose can inhibit the efficiency of photocatalytic degradation of TC. This may be due to the enhanced dispersion of light at higher catalyst dosages and the increased susceptibility of deposition and agglomeration of high-dose nanomaterials [55]. In addition, at higher catalyst loads, the accumulation and precipitation of the supported catalyst result in a decrease in the surface area of the available catalyst for photon absorption, thus reducing the degradation rate [56]. TiO_2 nano-material was used as a photocatalyst to degrade TC by Safari [57] et al. It was found that the dose of the photocatalyst was positively related to the degradation efficiency of TC.

When the catalyst dosage was higher than 100 mg/L, the photocatalytic degradation efficiency of TiO_2 on TC decreased. When the concentration of the pollutant is 20 mg/L, the composite catalyst has the best degradation effect on TC. The increase in the initial concentration of TC leads to the decrease in the degradation efficiency of TC, which may be due to the transition from low concentration to the mass transfer limitation of low concentration. Moreover, at higher concentrations, the hydroxyl group becomes a limiting reactant as the concentration of the intermediate increases, so the degradation rate and constant decrease [58]. In addition, with the increase in the initial concentration of TC, more TC molecules are adsorbed on the catalyst surface. A large amount of adsorbed TC leads to the inhibition of TC molecules on photopores or hydroxyl radicals. This can result from the increase in internal optical density, and the solution cannot pass through ultraviolet light [59]. In addition, the increased concentration of TC results in the absorption of light by TC molecules, which makes it difficult for photons to reach the surface of the photocatalyst and reduces the efficiency of photocatalysis removal [60]. These results are similar to those obtained by Chen et al. [61] and Ahmadi et al. [62]. The results showed that

the photocatalytic removal efficiency of TC decreased with increasing initial concentration of TC under visible light irradiation.

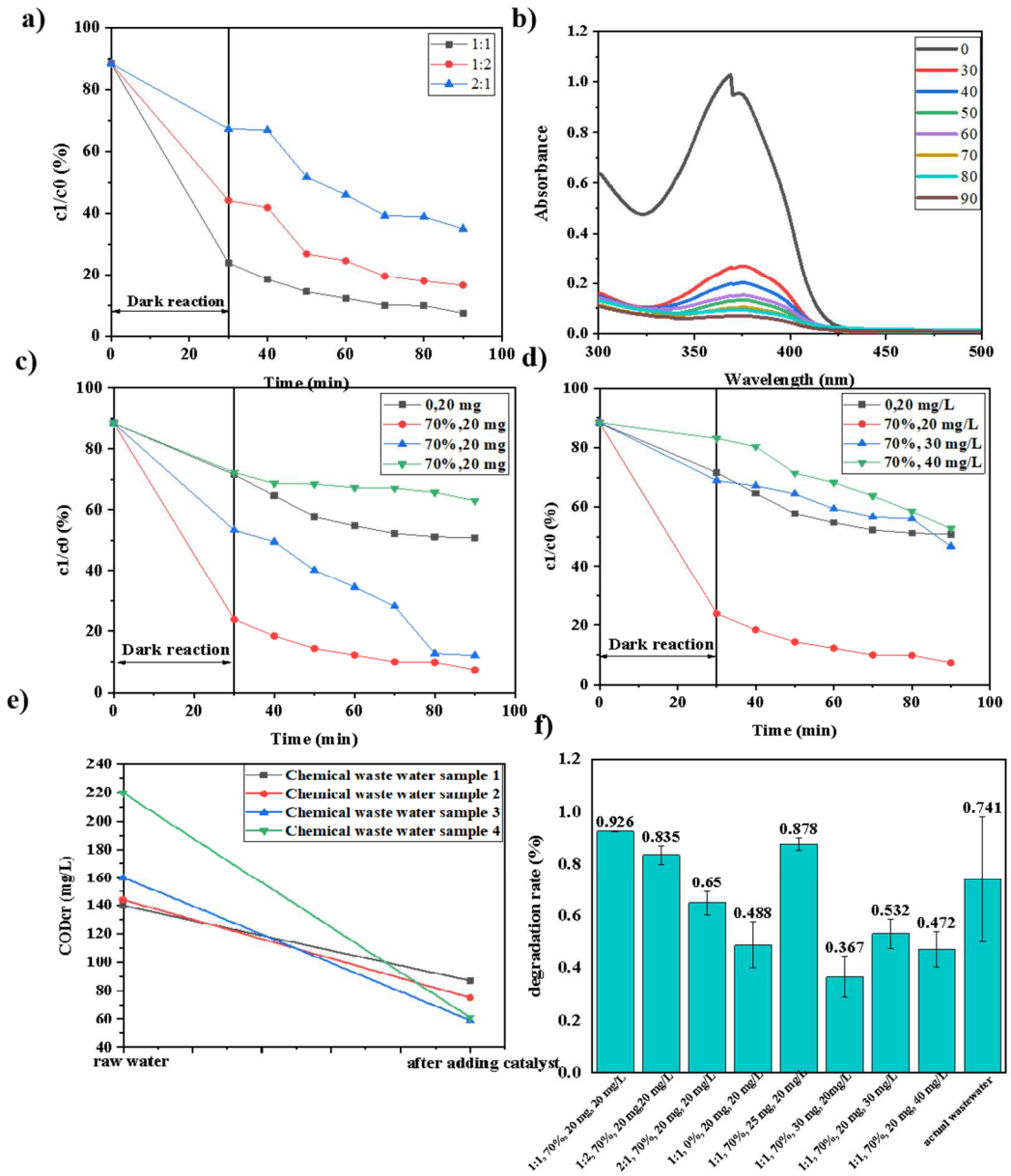

Figure 7. Selection of the best composition proportion (**a**); the absorbance curve of 1:1 optimum ratio catalyst at 350 nm wavelength (**b**); effect of different catalyst dosage on performance (**c**); effect of different concentration of TC on performance (**d**); degradation of CODcr in practical wastewater by catalyst (**e**); comparison of degradation rate of catalysts under different conditions (**f**).

Figure 7a,c,d show the photocatalytic activities of the materials under different reaction conditions. It can be seen that the main decrease in TC concentration occurred in the first 30 min of dark reaction and was due to the strong adsorption of the ZnO-C/MnO_2 catalyst. In order to explore the differences in the adsorption amounts of catalysts under different conditions in dark reaction, in this paper, comparative experiments are employed. As shown in Figure S1, comparing the conditions under different conditions without light effect, the same aeration amount, catalyst mass, and TC concentration when the mass ratio of catalyst ZnO-C and MnO_2 is 1:1, with too much catalyst mass or TC concentration and aeration affects the adsorption of TC by the catalyst, among which 20 mg ZnO-C/MnO_2 and 20 mg/L TC have the maximum adsorption. After 60 min, the TC concentration re-

mained almost unchanged under different conditions, which indicates that the adsorption equilibrium was reached. The adsorption alone did not achieve the post-photocatalytic degradation effect for the degradation of TC concentration, indicating that the photocatalytic part played a crucial role in the degradation of TC by ZnO-C/MnO_2 catalysts.

2.2.2. Degradation of Actual Petrochemical Wastewater

The practical degradation effect of the ZnO-C/MnO_2 catalyst with the optimum ratio of 1:1:1 was tested by degrading actual petrochemical wastewater with unknown and complicated components. Figure 7e shows the CODcr value before and after the petrochemical wastewater degradation measured by the national standard method of CODcr. It can be found from the graph that ZnO-C/MnO_2 catalytic material has a good degradation effect on the actual wastewater, which the minimum CODcr of 100 mg catalyst for actual petrochemical wastewater can be reduced to 59. Although the composition of petrochemical wastewater is complex and the CODcr measurement error is large, the comparison between the simulated wastewater and the actual wastewater degradation rate in Figure 7f shows that the material has certain practical applications.

2.3. Exploration of TC Transformation Pathway

To further explore the degradation mechanism of the ZnO-C/MnO_2 degradation TC process, the degradation products of the ZnO-C/MnO_2 photocatalytic process under the optimal conditions were determined by HPLC-MS analysis, and the TC mass spectra at different reaction times (0 min, 30 min, and 60 min) are shown in Figure 8. There were five main degradation products of TC (in Table 2), and their possible translational degradation pathways were speculated to be shown in Figure 9. M/Z = 445 of TC, after attack by $^{\bullet}OH$ radicals, firstly decomposed into the products at M/Z = 388, M/Z = 372 and M/Z = 330, and then decomposed into the products at M/Z = 279 by demethylation and carbon–carbon single-bond cleavage reactions, finally changing into CO_2 and H_2O.

2.4. Photocatalysis Mechanism

2.4.1. Analysis of Heterostructure

To explore the configuration of heterostructures, XPS diagrams have been used to analyze the heterostructures. Zn loses electrons in the 2P orbit, Mn obtains electrons in the 2P orbit, and C acts as the intermediate for auxiliary electron transfer. It can be inferred that the type of heterojunction may be type-II, type-Z, or type-S.

For the purpose of further exploring the types of heterojunction, the free radical trapping experiments were carried out on ZnO-C/MnO_2 catalyst to explore the electron transfer mechanism. In this experiment, 5,5-dimethyl-1-pyrrolidine nitrogen oxide (DMPO) was used as spin trapping agent for EPR analysis. In Figure 10a, in the absence of light, the signal of $^{\bullet}O_2^{-}$ was not detected, but a quadruple signal of 1:1:1 was observed after the sample was irradiated by simulated sunlight. A similar phenomenon can be observed for $^{\bullet}OH$ (Figure 10b), and the gradually enhanced 1:2:2:1 characteristic signals were detected when the light was on. The results of trapping experiment and EPR experiment suggest that $^{\bullet}O_2^{-}$ and $^{\bullet}OH$ radicals produced by ZnO-C/MnO_2 composites under light are the main active components in the process of photocatalytic degradation. Significantly, if the charge transfer in the composite follows the traditional type-II heterojunction mechanism, and due to the requirements of S-type reduction potential and oxidation potential being higher, $^{\bullet}O_2^{-}$ free radicals cannot be generated so it cannot be an S-type heterojunction. It is obvious that the heterojunction mechanism of Z-scheme can better explain the enhancement mechanism of photocatalytic degradation activity of ZnO-C/MnO_2 composite photocatalyst. Because ZnO-C/MnO is a ternary composite and C acts as a two-sided mediator for electron transfer, the heterojunction type of the catalyst can be defined as all-solid Z-scheme heterojunction.

Table 2. Intermediate determined in the degradation of TC by ZnO-C/MnO_2.

Compound	$[M+H]^+$	Molecular Formula	Molecular Structural Formula
TC	445	$C_{22}H_{24}O_8N_2$	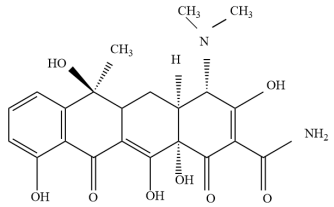
1	388	$C_{20}H_{20}O_8$	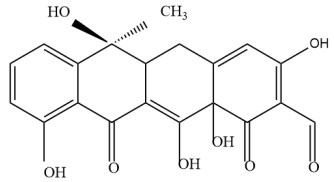
2	372	$C_{20}H_{21}O_6N$	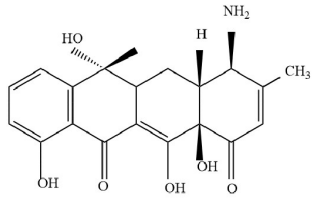
3	330	$C_{19}H_{22}O_5$	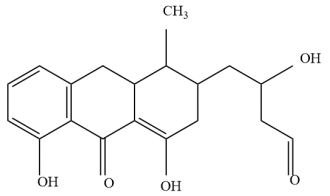
4	304	$C_{20}H_{16}O_3$	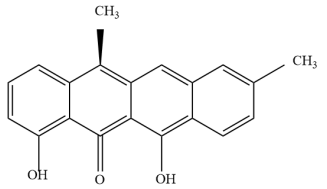
5	279	$C_{15}H_{21}O_4N$	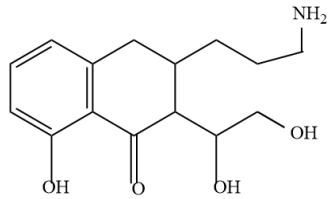

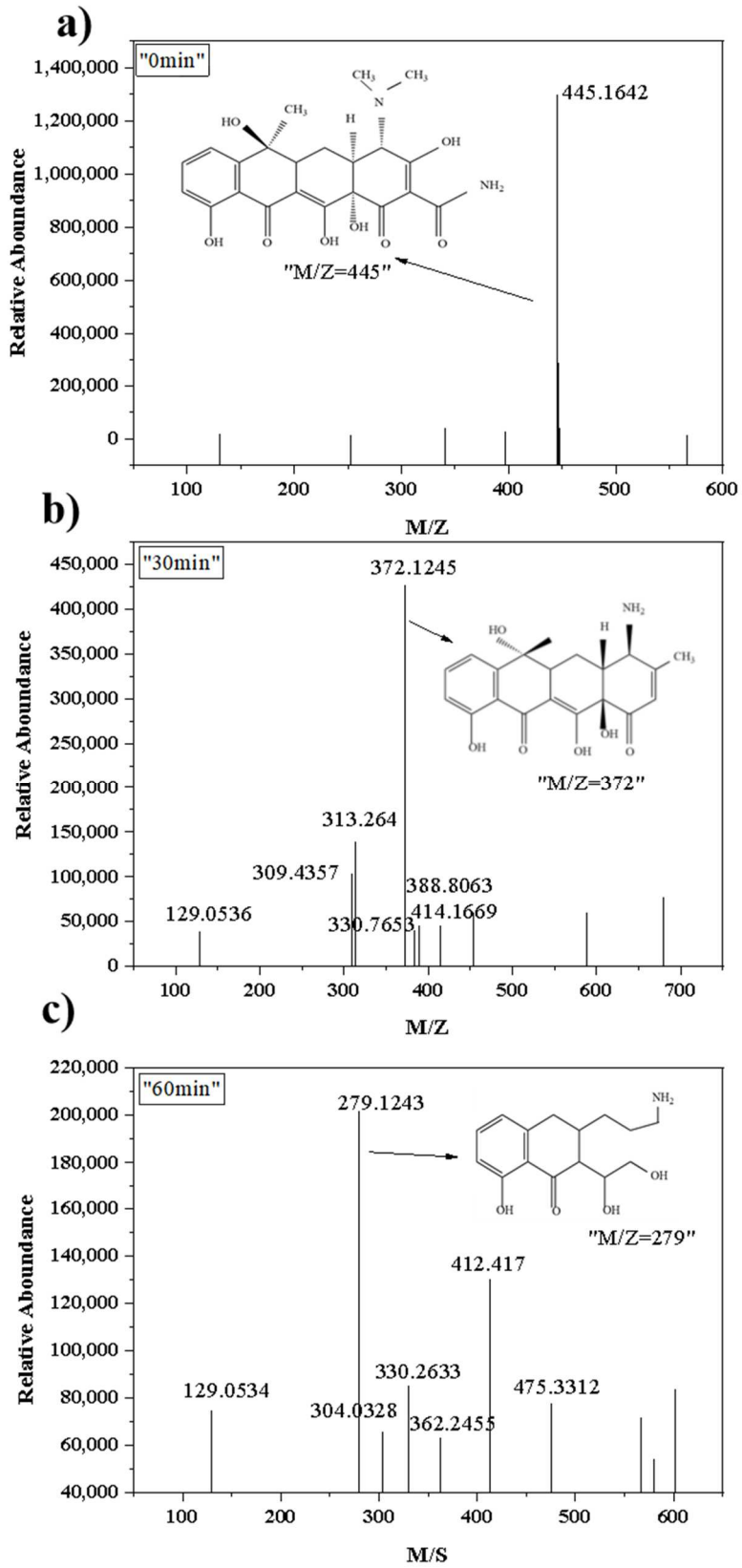

Figure 8. ZnO-C/MnO_2 processing TC mass spectrum. (**a**) 0 min; (**b**) 30 min; (**c**) 60 min.

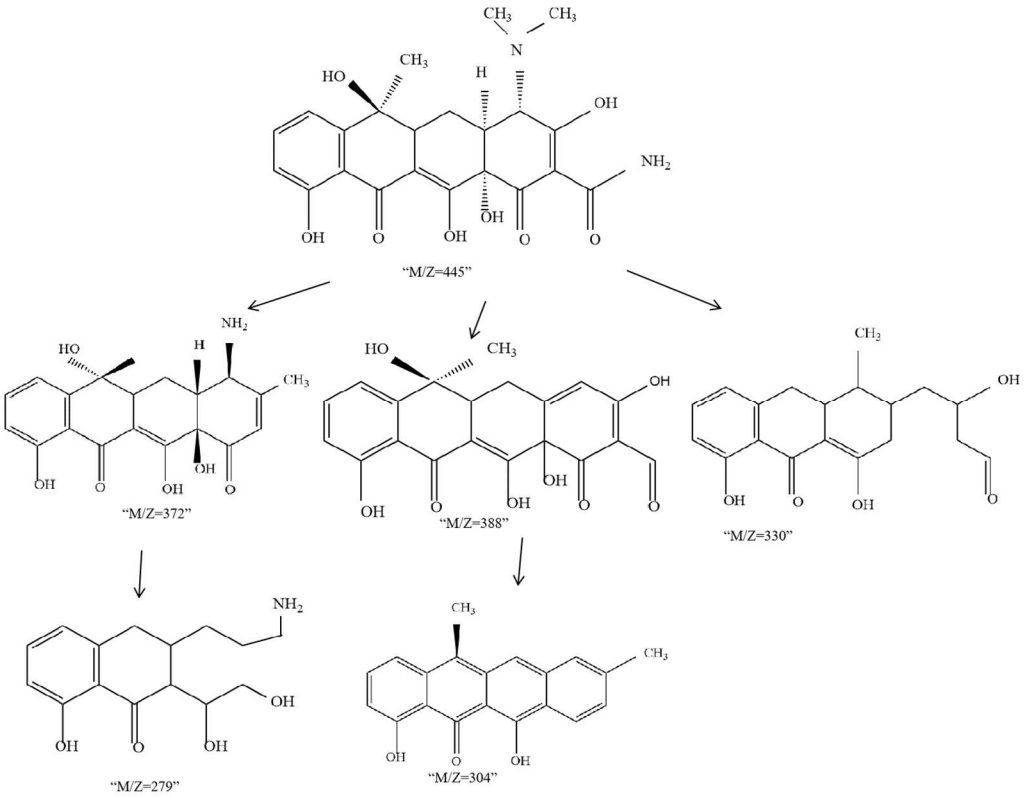

Figure 9. Degradation pathway of TC.

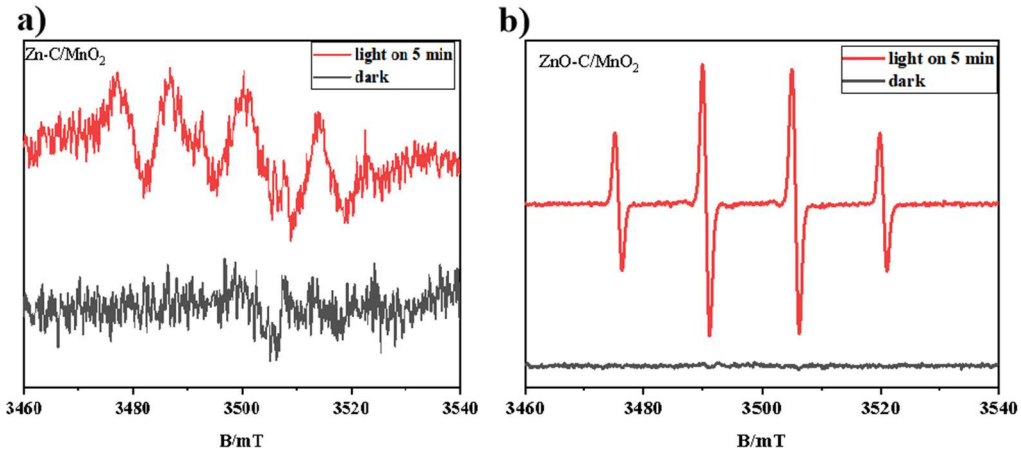

Figure 10. EPR spectra of ZnO-C/MnO_2 under dark and simulated solar light: DMPO $^{\bullet}O_2^{-}$ (**a**) in methanol dispersions and DMPO $^{\bullet}$OH; (**b**) in aqueous dispersions.

It is well-known that the direction of electron transfer at a heterogeneous interface correlates with the work function of a semiconductor [63,64]. Figure 11 shows the mechanism of carrier transport between ZnO, C, and MnO_2. In Figure 11a, since the work function of ZnO (W_1) is larger than that of MnO_2 (W_2), when ZnO and MnO_2 come into contact, the electrons spontaneously transfer from MnO_2 to ZnO at the two-phase interface, resulting in a positive charge on one side of MnO_2, a negative charge on the other side of ZnO, and a balance at last; thus, an internal electric field is formed as shown in Figure 12b. Then, as shown in Figure 11c, the valence electrons of ZnO and MnO_2 are excited into the conduction band under illumination. Under the action of the built-in electric field, the photoelectrons in the ZnO conduction band and the photoholes in MnO_2 compound at the interface, forming a direct Z-scheme heterostructure, facilitates efficient separation of photocarriers [65]. When C and MnO_2 are in contact and equilibrium on ZnO surface, they form heterojunction. Under

illumination, the electron excitation transitions to the conduction band C of MnO_2 and the heterojunction prevents the electron from reentering MnO_2, thus effectively facilitating the photocarrier separation. Finally, as shown in Figure 12d, when ZnO-C/MnO_2 is excited by light, C becomes the composite center of the conduction band electron of MnO_2 and the valence band hole of ZnO, forming a typical Z-scheme carrier transport mechanism, which is beneficial to the photocarrier separation in the catalytic system.

2.4.2. Analysis of Photocatalysis Mechanism

Based on the above results, the photocatalytic mechanism of ZnO-C/MnO_2 nanocomposites prepared in this experiment is shown in Figure 12. When ZnO-C absorbs ultraviolet radiation under simulated solar radiation, electrons are excited to jump from the valence band to the conduction band, and leave the same number of holes in the valence band. The visible light which cannot be absorbed by ZnO can reach the surface of MnO_2. Due to the narrow bandgap of MnO_2, the visible light can be absorbed and the photoelectron-hole pair can be formed inside the MnO_2. In this way, ZnO-C/MnO_2 composite nano-materials can extend the light utilization range from the ultraviolet region to the visible region, and improve the utilization ratio of sunlight. The CB (less reductive) electrons of ZnO and the VB (less oxidizing) holes of MnO_2 were transferred to C and rapidly compounded. In contrast, the VB holes in ZnO (strong oxidation ability) and the electrons on the CB of MnO_2 (strong reduction ability) remained. In this way, it is possible to separate the electrons with a strong oxidation-reduction ability from the holes. On the one hand, the electrons on the CB of ZnO combine with O_2 adsorbed on the surface of the catalyst to produce $^{\bullet}O_2^{-}$, and further combine with the protons to form $^{\bullet}OH$, $^{\bullet}O_2^{-}$ and $^{\bullet}OH$, which are the active species for the oxidative degradation of TC. On the other hand, the strong oxidation hole (h^+) on the VB of MnO_2 can degrade TC directly. Therefore, for ZnO-C/MnO_2 catalyst, the co-action of ZnO and surface plasma C greatly accelerated the degradation of TC under visible light irradiation. The photoelectrons react with O_2 and water molecules adsorbed on the surface to form $^{\bullet}O_2^{-}$ and $^{\bullet}OH$ radicals. Moreover, the holes in the ZnO valence band can react with the $^{\bullet}OH$ in the solution to form the highly oxidized $^{\bullet}OH$. The $^{\bullet}OH$ reacts with TC and oxidizes it to inorganic small molecules such as H_2O and CO_2.

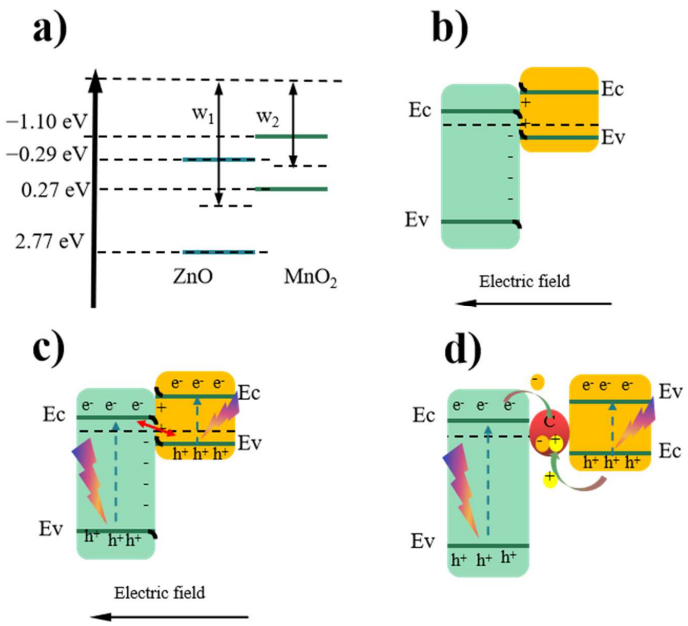

Figure 11. ZnO, MnO_2 band structure (**a**); ZnO and MnO_2 charge distribution on contact (**b**); ZnO and MnO_2 carrier transport mechanism (**c**); ZnO-C/MnO_2 heterojunction Z-scheme carrier transport mechanism (**d**).

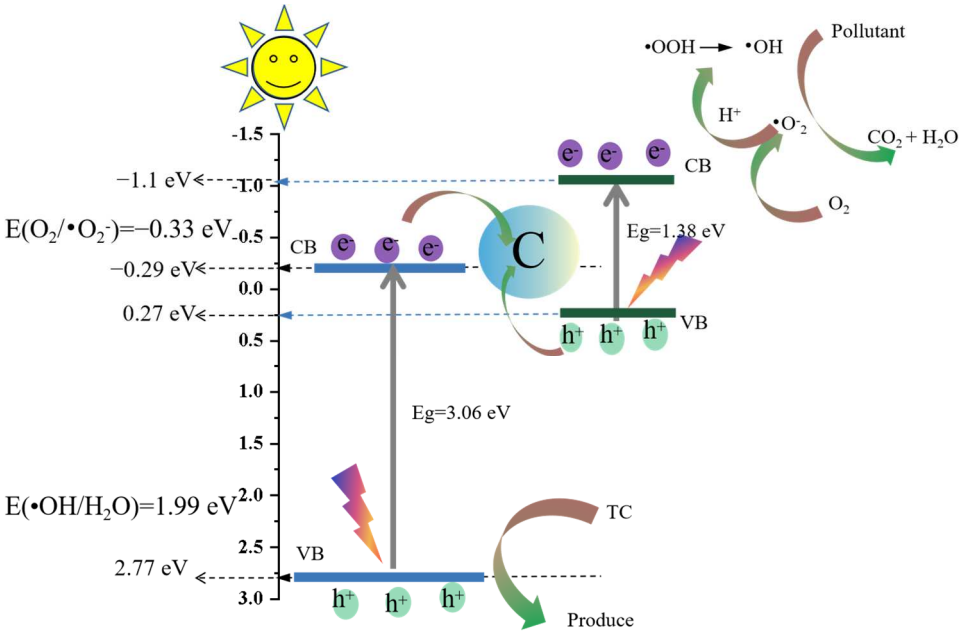

Figure 12. Photocatalytic mechanism of ZnO-C/MnO_2 all-solid Z heterojunction.

3. Experimental

3.1. Materials

Ethanol, ethylene glycol, zinc acetate dihydrate, manganese sulfate, potassium permanganate were all purchased by Aladdin. Pure water with resistivity greater than 18.25 MΩ/cm was used in all experiments, and all chemical reagents were classified and used according to standards.

3.2. Preparation of ZnO-C

Mix 5 mL ethylene glycol and 75 mL ethanol and stir for 30 min, and then add 0.654 g zinc acetate dihydrate to the mixture. After stirring for 30 min, the transparent solution was transferred into a 100 mL Teflon lined stainless steel autoclave and heated at 180 °C for 12 h. Sediments are separated by centrifugation, washed with anhydrous ethanol and dried at 60 °C for 12 h. Finally, the samples were annealed at 400 °C for 1 h with a heating rate of 5 °C /min.

3.3. Preparation of MnO_2

Add 0.442 g manganese sulfate and 0.354 g potassium permanganate to 15 mL deionized water, stir well for 30 min. The transparent solution was transferred into a 100 mL Teflon lined stainless steel autoclave and heated at 160 °C for 6 h. The precipitate was separated by centrifugation, washed with absolute ethanol and dried at 60 °C for 12 h.

3.4. Preparation of ZnO-C/MnO_2

As shown in Figure 13, MnO_2 prepared and ZnO-C dried at 60 °C for 6 h are ground evenly according to a certain mass ratio, and annealed at 400 °C for 1 h at a heating rate of 5 °C/min.

3.5. Photocatalytic Tests

The catalyst was first weighed at 20 mg and prepared 20 mol/L tetracycline hydrochloride (TC) solution, then the catalyst was placed in 100 mL TC solution, the solution was dark treated with aeration for 30 min, and the solution was sampled before and after 30 min. After light treatment with halogen lamp (340 nm–800 nm), samples were taken every 10 min and observed for 1 h. Measuring spectrophotometric curve.

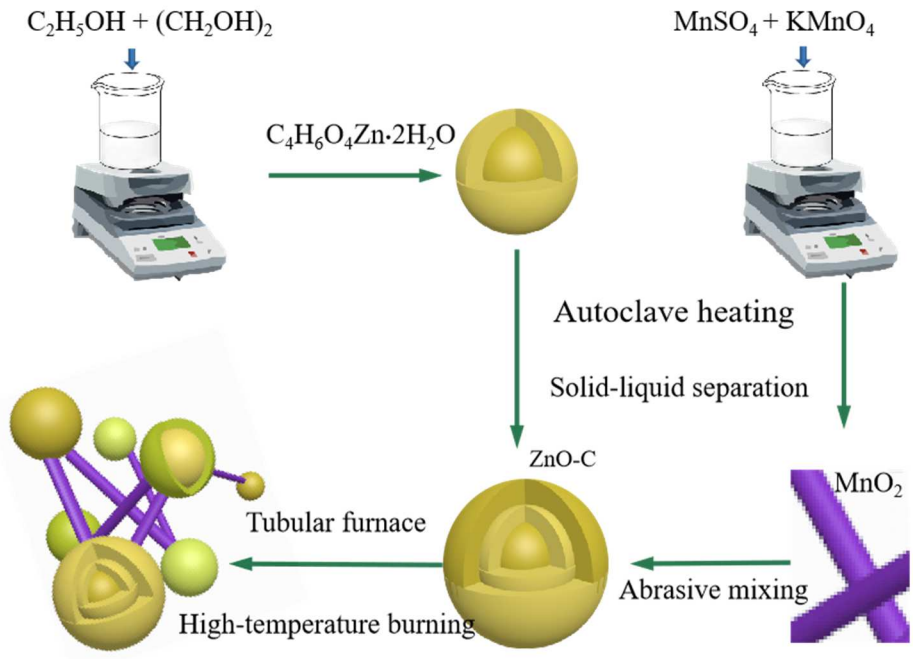

Figure 13. Flow chart of material preparation.

3.6. Characterizations

X-ray diffraction (XRD, Bruker, D8, Karlsruhe, Germany) patterns were recorded in X Pert-Pro MPD/max-γOn a X-ray diffractometer, cukx radiation is adopted (λ = 0.154 nm). The lattice spacing was measured using a high-resolution transmission electron microscope (TEM, FEI Talos F200x, Thermo Fischer Scientific, Waltham, MA, USA). The surface morphology and elemental analysis were analyzed by field emission scanning electron microscopy (SEM, ZEISS Gemini 300, ZEISS, Oberkochen, Germany) and energy dispersive spectroscopy (EDS). X-ray photoelectron spectroscopy (XPS, Thermo Fisher Nexsa) uses Mono AlKa (hν = 1200 eV). The current density time curve (I-T) was measured in a self-made three electrode battery at CHI660E electrochemical station of Chenhua company in Shanghai, China. Ultraviolet visible diffuse reflectance spectroscopy (UV-Vis DRS, Shimadzu UV-3600, Shimadzu Corp., Kyoto, Japan) and Mott Schottky (M-S) measure the type, current density and flat band potential of semiconductors. Combined with ultraviolet visible diffuse reflectance spectroscopy, the conduction band and valence band position of semiconductors can also be calculated. The photoluminescence (PL) spectrum of the sample was measured using a fluorescence spectrometer (Hitachi F-7000, Hitachi Ltd., Chiyoda, Japan) with an excitation wavelength of 370 nm. Electron paramagnetic resonance (EPR, Bruker EMX plus, Bruker, Billerica, MA, USA) analysis was performed using 5,5-dimethyl-1-pyrrolidine nitrogen oxide (DMPO) as spin trapping agent, with a central field of 3502.00 G.

4. Conclusions

To sum up, the ternary composite catalyst ZnO-C/MnO_2 was successfully prepared by hydrothermal synthesis in this study, and the composition and photocatalytic mechanism of all-solid Z-scheme heterojunction were demonstrated by XPS, SEM, and other experiments. Compared with the common Z-scheme heterojunction, the catalyst in this paper uses doping technology, using common element C rather than precious metals such as electron transport media, thus improving the photocatalytic efficiency of the catalyst. It can be seen from many comparative experiments that besides the advantages of low cost and simple preparation, ZnO-C/MnO_2 catalyst can degrade both simulated antibiotic wastewater and actual petrochemical wastewater considerably. At present, with all kinds of catalysts in full bloom, the preparation of simple, low-cost, and high-performance catalysts such as

ZnO-C/MnO_2 will become the first choice for the degradation of pollutants. In addition, the combination of doping technology, core shell structure, and heterojunction provides more possibilities for the composition of catalysts.

Supplementary Materials: The following supporting information can be downloaded at: https://www.mdpi.com/article/10.3390/catal12101250/s1, Figure S1: Adsorption of TC by ZnO-C/MnO_2 Catalyst under Different Conditions in Dark Reaction.

Author Contributions: Formal analysis, H.G.; investigation, Y.Z.; resources, J.Z.; data curation, B.Y.; writing—original draft preparation, L.Z.; writing—review and editing, T.Y. (Tingting Yu); visualization, M.W.; supervision, T.Y. (Tao Yang); project administration, L.L.; funding acquisition, C.G. All authors have read and agreed to the published version of the manuscript.

Funding: This study was supported by the Natural Science Foundation of Jiangsu Province (Grant No. BK20181074) and funded by China Postdoctoral Science Foundation (2021M691327). It was also funded by Jiangsu Postdoctoral Science Foundation (2021K313C), Lianyungang Postdoctoral Research Foundation and Postgraduate Research and Practice Innovation Program of Jiangsu Province (KYCX20_2925). Supported by the Priority Academic Program Development of Jiangsu Higher Education Institutions (No. JSIMR202013) and Jiangsu Ocean University talent introduction start-up fund (No. KQ18005) along with Major Scientific and Technological Innovation Projects of Key R&D Programs in Shandong Province, China (2019JZZY020234).

Data Availability Statement: The datasets used and analyzed during the current study are available from the corresponding references listed.

Conflicts of Interest: The authors declare no conflict of interest.

References

1. Li, Z.-X.; Bao, Z.-Y.; Yao, F.-Y.; Cao, H.-Q.; Wang, J.-H.; Qiu, L.; Lv, J.; Sun, X.; Zhang, Y.; Wu, Y.-C. One-dimensional bismuth vanadate nanostructures constructed Z-scheme photocatalyst for highly efficient degradation of antibiotics. *J. Water Process Eng.* **2022**, *46*, 102599. [CrossRef]
2. Zhang, L.; Bai, J.-H.; Wang, C.; Wei, Z.-Q.; Wang, Y.-Q.; Zhang, K.-G.; Xiao, R.; Jorquera, M.A.; Acuña, J.J.; Campos, M. Fate and ecological risks of antibiotics in water-sediment systems with cultivated and wild Phragmites australis in a typical Chinese shallow lake. *Chemosphere* **2022**, *305*, 135370. [CrossRef] [PubMed]
3. Zhou, L.; Li, S.-N.; Li, F.-X. Damage and elimination of soil and water antibiotic and heavy metal pollution caused by livestock husbandry. *Environ. Res.* **2022**, *215*, 114188. [CrossRef] [PubMed]
4. Han, S.; Xiao, P.-F. Catalytic degradation of tetracycline using peroxymonosulfate activated by cobalt and iron Co-loaded pomelo peel biochar nanocomposite: Characterization, performance and reaction mechanism. *Sep. Purif. Technol.* **2022**, *287*, 120533. [CrossRef]
5. Tang, S.; Lin, L.-J.; Wang, X.-S.; Yu, A.-Q.; Sun, X. Interfacial interactions between collected nylon microplastics and three divalent metal ions (Cu(II), Ni(II), Zn(II)) in aqueous solutions. *J. Hazard. Mater.* **2021**, *403*, 123548. [CrossRef]
6. Lin, L.-J.; Tang, S.; Wang, X.-S.; Sun, X.; Han, Z.-X.; Chen, Y. Accumulation mechanism of tetracycline hydrochloride from aqueous solutions by nylon microplastics. *Environ. Technol. Innov.* **2020**, *18*, 100750. [CrossRef]
7. Peng, J.-B.; Wang, Z.-X.; Wang, S.-Y.; Liu, J.; Zhang, Y.-Z.; Wang, B.-J.; Gong, Z.-M.; Wang, M.-J.; Dong, H.; Shi, J.-L.; et al. Enhanced removal of methylparaben mediated by cobalt/carbon nanotubes (Co/CNTs) activated peroxymonosulfate in chloride-containing water: Reaction kinetics, mechanisms and pathways. *Chem. Eng. J.* **2021**, *409*, 128176. [CrossRef]
8. Jin, X.-K.; Chen, J.-J.; Chen, F.-J.; Duan, H.-M.; Wang, Z.-Y.; Li, J.-H. Solid-State Synthesis of ZnO/ZnS Photocatalyst with Efficient Organic Pollutant Degradation Performance. *Catalysts* **2022**, *12*, 981. [CrossRef]
9. Zhao, J.-Y.; Sun, J.-P.; Meng, X.-C.; Li, Z.-Z. Recent Advances in Vehicle Exhaust Treatment with Photocatalytic Technology. *Catalysts* **2022**, *12*, 1051. [CrossRef]
10. Dai, Y.-H.; Cao, H.; Qi, C.-D.; Zhao, Y.-J.; Wen, Y.-N.; Xu, C.-M.; Zhong, Q.; Sun, D.-Y.; Zhou, S.-H.; Yang, B.; et al. L-cysteine boosted Fe(III)-activated peracetic acid system for sulfamethoxazole degradation: Role of L-cysteine and mechanism. *Chem. Eng. J.* **2023**, *451*, 138588. [CrossRef]
11. Cao, F.; Wang, T.; Ji, X.-H. Enhanced visible photocatalytic activity of tree-like ZnO/CuO nanostructure on Cu foam. *Appl. Surf. Sci.* **2019**, *471*, 417–424. [CrossRef]
12. Ashoka, S.; Chithaiah, P.; Thipperudraiah, K.V.; Chandrappa, G.T. Nanostructural zinc oxide hollow spheres: A facile synthesis and catalytic properties. *Inorg. Chim. Acta* **2010**, *363*, 3442–3447. [CrossRef]
13. Goktas, A.; Modanlı, S.; Tumbul, A.; Kilic, A. Facile synthesis and characterization of ZnO, ZnO: Co, and ZnO/ZnO: Co nano rod-like homojunction thin films: Role of crystallite/grain size and microstrain in photocatalytic performance. *J. Alloys Compd.* **2022**, *893*, 162334. [CrossRef]

14. Vasantharaj, S.; Sathiyavimal, S.; Senthilkumar, P.; Kalpana, V.N.; Rajalakshmi, G.; Alsehli, M.; Elfasakhany, A.; Pugazhendhi, A. Enhanced photocatalytic degradation of water pollutants using bio-green synthesis of zinc oxide nanoparticles (ZnO NPs). *J. Environ. Chem. Eng.* **2021**, *9*, 105772. [CrossRef]
15. Borsagli, F.J.L.M.; Paiva, A.E. Eco-friendly luminescent ZnO nanoconjugates with thiol group for potential environmental photocatalytic activity. *J. Environ. Chem. Eng.* **2021**, *9*, 105491. [CrossRef]
16. Dai, Y.-H.; Qi, C.-D.; Cao, H.; Wen, Y.-N.; Zhao, Y.-J.; Xu, C.-M.; Yang, S.-G.; He, H. Enhanced degradation of sulfamethoxazole by microwave-activated peracetic acid under alkaline condition: Influencing factors and mechanism. *Sep. Purif. Technol.* **2022**, *288*, 20716. [CrossRef]
17. Zhao, W.-X.; Liu, S.; Zhang, S.; Wang, R.; Wang, K.-Q. Preparation and visible-light photocatalytic activity of N-doped TiO_2 by plasma-assisted sol-gel method. *Catal. Today* **2019**, *337*, 37–43. [CrossRef]
18. Wang, S.-B.; Zhang, X.-W.; Li, S.; Fang, Y.; Pan, L.; Zou, J.-J. C-doped ZnO ball-in-ball hollow microspheres for efficient photocatalytic and photoelectrochemical applications. *J. Hazard. Mater.* **2017**, *331*, 235–245. [CrossRef]
19. Li, Y.-Y.; Liang, S.-Y.; Sun, H.-H.; Hua, W.; Wang, J.-G. Defect Engineering and Surface Polarization of TiO_2 Nanorod Arrays toward Efficient Photoelectrochemical Oxygen Evolution. *Catalysts* **2022**, *12*, 1021. [CrossRef]
20. Wang, H.-W.; Yu, T.-T.; Li, Y.-H.; Liu, L.-F.; Gao, C.-F.; Ding, J. Self-sustained bioelectrical reduction system assisted iron–manganese doped metal-organic framework membrane for the treatment of electroplating wastewater. *J. Clean. Prod.* **2022**, *331*, 129972. [CrossRef]
21. Zhu, W.-R.; Hao, N.; Yang, X.-D. Study on the determination of glucose based on manganese dioxide-oxygen-doped carbon nitride, coenzyme-free colorimetry. *Anal. Chem.* **2020**, *48*, 727–732.
22. Liu, Y.-G.; Li, Z.-G.; Chen, W.-Z. Enzyme-free hydrogen peroxide sensor based on prussian manganese dioxide composite modified electrode. *J. Inorg. Chem.* **2020**, *36*, 421–425.
23. Belousov, A.S.; Suleimanov, E.V.; Parkhacheva, A.A.; Fukina, D.G.; Koryagin, A.V.; Koroleva, A.V.; Zhizhin, E.V.; Gorshkov, A.P. Regulating of MnO_2 photocatalytic activity in degradation of organic dyes by polymorphic engineering. *Solid State Sci.* **2022**, *132*, 106997. [CrossRef]
24. Çakıroğlu, B.; Demirci, Y.C.; Gökgöz, E.; Özacar, M. A photoelectrochemical glucose and lactose biosensor consisting of gold nano- particles, MnO_2 and g-C_3N_4 decorated TiO_2. *Sens. Actuators B Chem.* **2019**, *282*, 282–289. [CrossRef]
25. Majumder, T.; Dhar, S.; Debnath, K.; Mondal, S.P. Role of S, N co-doped graphene quantum dots as a green photosensitizer with Ag-doped ZnO nanorods for improved electrochemical solar energy conversion. *Mater. Res. Bull.* **2017**, *93*, 214–222. [CrossRef]
26. Mika, K.; Syrek, K.; Uchacz, T.; Sulka, G.D.; Zaraska, L. Dark nanostructured ZnO films formed by anodic oxidation as photoanodes in photoelectrochemical water splitting. *Electrochimica Acta* **2022**, *414*, 140176. [CrossRef]
27. Chiam, S.L.; Pung, S.Y.; Yeoh, F.Y. Recent developments in MnO_2-based photocatalysts for organic dye removal: A review. *Environ. Sci. Pollut. Res.* **2020**, *27*, 5759–5778. [CrossRef]
28. Lu, Y.-Q.; Ding, C.-S.; Guo, J.; Gan, W.; Chen, P.; Zhang, M.; Sun, Z.-Q. Highly efficient photodegradation of ciprofloxacin by dual Z-scheme Bi_2MoO_6/GQDs/TiO_2 heterojunction photocatalysts: Mechanism analysis and pathway exploration. *J. Alloys Compd.* **2022**, *924*, 166533. [CrossRef]
29. Saud Athar, M.; Danish, M.; Muneer, M. Fabrication of visible light-responsive dual Z-Scheme (α-Fe_2O_3/CdS/g-C_3N_4) ternary nanocomposites for enhanced photocatalytic performance and adsorption study in aqueous suspension. *J. Environ. Chem. Eng.* **2021**, *9*, 105754. [CrossRef]
30. Yu, T.-T.; Liu, Q.-S.; Chen, G.; Liu, L.-F.; Zhang, J.-L.; Gao, C.-F.; Yang, T. Microbial coupled photocatalytic fuel cell with a double Z-scheme g-C_3N_4/ZnO/$Bi_4O_5Br_2$ cathode for the degradation of different organic pollutants. *Int. J. Hydrog. Energy* **2022**, *47*, 3781–3790. [CrossRef]
31. Jia, X.-W.; Wang, C.; Li, Y.-F.; Zhang, R.-Y.; Shi, Z.; Liu, X.-C.; Yu, X.-D.; Zhang, M.; Xing, Y. All-Solid-State Z-scheme Ta_3N_5/Bi/$CaTaO_2N$ photocatalyst transformed from perovskite $CaBi_2Ta_2O_9$ for efficient overall water splitting. *Chem. Eng. J.* **2022**, *431*, 134041. [CrossRef]
32. Zhang, M.; Yin, H.-F.; Yao, J.-C.; Arif, M.; Qiu, B.; Li, P.-F.; Liu, X.-H. All-solid-state Z-scheme BiOX(Cl, Br)-Au-CdS heterostructure: Photocatalytic activity and degradation pathway. *Colloids Surf. A Physicochem. Eng. Asp.* **2020**, *602*, 124778. [CrossRef]
33. Jia, K.; Liu, G.; Lang, D.-N.; Chen, S.-F.; Yang, C.; Wu, R.-L.; Wang, W.; Wang, J.-D. Degradation of tetracycline by visible light over ZnO nanophotocatalyst. *J. Taiwan Inst. Chem. Eng.* **2022**, *136*, 104422. [CrossRef]
34. Shaly, A.A.; Priya, G.H.; Matharasi, A.; Prabha, A.S.; Linet, J.M. The nature and role of α-MnO_2 nanowires in the photocatalytic degradation of the antibiotic tetracycline. *Mater. Today Proc.* **2022**, *5*, 174.
35. Liu, R.; Zuo, D.-Y.; Tan, C. Construction of C/ZnO/BiOI photocatalyst for enhanced degradation of carbaryl: Characterization, performance and mechanism. *J. Alloys Compd.* **2022**, *911*, 165023. [CrossRef]
36. Zou, J.; Wu, K.; Wu, H.-D.; Guo, J.; Zhang, L.-F. Synthesis of heterostructure δ-MnO_2/h-MoO_3 nanocomposite and the enhanced photodegradation activity of methyl orange in aqueous solutions. *J. Mater. Sci.* **2020**, *55*, 3329–3346. [CrossRef]
37. Ma, M.-L.; Chen, Y.; Jiang, J.B.; Bi, Y.-X.; Liao, Z.-J.; Ma, Y. One-dimensional recoverable $ZnFe_2O_4$/C/MnO_2/BiOI magnetic composite with enhanced photocatalytic performance for organic dyes degradation. *Environ. Sci. Pollut. Res.* **2022**, *29*, 63233–63247. [CrossRef]
38. Gao, Y.-Y.-X.; Li, L.; Zu, W.L.; Sun, Y.-G.; Gun, J.H.; Cao, Y.Z.; Yu, H.X.; Zhang, W.-Z. Preparation of Dual Z-scheme Bi_2MoO_6/$ZnSnO_3$/ZnO Heterostructure Photocatalyst for Efficient Visible Light Degradation of Organic Pollutants. *J. Inorg. Organomet. Polym.* **2022**, *32*, 1840–1852. [CrossRef]

39. Ma, M.-L.; Yang, Y.-Y.; Chen, Y.; Jiang, J.-B.; Ma, Y.; Wang, Z.-F.; Huang, W.-B.; Wang, S.-S.; Liu, M.-Q.; Ma, D.-X.; et al. Fabrication of hollow flower-like magnetic $Fe_3O_4/C/MnO_2/C_3N_4$ composite with enhanced photocatalytic activity. *Sci. Rep.* **2021**, *11*, 2597. [CrossRef]
40. Luo, Q.-Z.; Sun, Y.-H.; Lv, X.; Huang, L.; Fang, L.; Wang, R. Creation of direct Z-scheme Al/Ga co-doping biphasic ZnO/g-C_3N_4 heterojunction for the sunlight-driven photocatalytic degradations of methylene blue. *J. Sol-Gel. Sci. Technol.* **2022**, *103*, 876–889. [CrossRef]
41. Zhou, Q.-J.; Zhang, L.-Z.; Zuo, P.J.; Wang, Y.; Yu, Z.-J. Enhanced photocatalytic performance of spherical BiOI/MnO_2 composite and mechanism investigation. *RSC Adv.* **2018**, *8*, 36161–36166. [CrossRef] [PubMed]
42. Zhang, G.-P.; Chen, D.Y.; Li, N.J.; Xu, Q.-F.; Li, H.; He, J.-H.; Lu, J.-M. Preparation of $ZnIn_2S_4$ nanosheet-coated CdS nanorod heterostructures for efficient photocatalytic reduction of Cr(VI). *Appl. Catal. B Environ.* **2018**, *232*, 164–174. [CrossRef]
43. Yang, Y.-S.; Zhang, Y.; Gou, C.-S.; Wu, W.-J.; Wang, H.; Zeng, Q.-R. Solar photocatalytic degradation of thidiazuron in Yangtze river water matrix by Ag/AgCl-AC at circumneutral condition. *Environ. Sci. Pollut. Res. Vol.* **2020**, *27*, 40857–40869. [CrossRef] [PubMed]
44. Chang, Y.-C.; Chiao, Y.-C.; Fun, Y.-X. Cu_2O/CuS/ZnS Nanocomposite Boosts Blue LED-Light-Driven Photocatalytic Hydrogen Evolution. *Catalysts* **2022**, *12*, 1035. [CrossRef]
45. Meda, U.S.; Vora, K.; Athrey, Y.; Mandi, U.A. Titanium dioxide based heterogeneous and heterojunction photocatalysts for pollution control applications in the construction industry. *Process Saf. Environ. Prot.* **2022**, *161*, 771–787. [CrossRef]
46. Qi, C.-D.; Wen, Y.-N.; Zhao, Y.-J.; Li, Y.-P.; Xu, C.-M.; Yang, S.-G.; He, H. Enhanced degradation of organic contaminants by Fe(III)/peroxymonosulfate process with l-cysteine. *Chin. Chem. Lett.* **2022**, *33*, 2125–2128. [CrossRef]
47. Zhang, B.; Hu, X.-Y.; Liu, E.-Z.; Fan, J. Novel S-scheme 2D/2D BiOBr/g-C_3N_4 heterojunctions with enhanced photocatalytic activity. *Chin. J. Catal.* **2021**, *42*, 1519–1529. [CrossRef]
48. Mohamed, R.-G.; Fan, H.-Q.; Ian, H.-L. Room-temperature solid state synthesis of Co_3O_4/ZnO p-n heterostructure and its photocatalytic activity. *Adv. Powder Technol.* **2017**, *28*, 953–963. [CrossRef]
49. Yao, S.-Y.; Wang, S.-Y.; Liu, R.-C. Delocalizing the d-electrons spin states of Mn site in MnO_2 for anion-intercalation energy storage. *Nano Energy* **2022**, *99*, 107391. [CrossRef]
50. Kim, D.; Yong, K. Boron doping induced charge transfer switching of a C_3N_4/ZnO photocatalyst from Z-scheme to type II to enhance photocatalytic hydrogen production. *Appl. Catal. B Environ.* **2021**, *282*, 119538. [CrossRef]
51. Liu, Z.-H.; Cai, X.-N.; Fan, S.-L.; Zhang, Y.-J.; Hu, H.-Y.; Huang, Z.-Q.; Liang, J.; Qin, Y.-B. Preparation of a stable polyurethane sponge supported Sn-doped ZnO composite via double-template-regulated bionic mineralization for visible-light-driven photocatalytic degradation of tetracycline. *J. Environ. Chem. Eng.* **2021**, *9*, 105541. [CrossRef]
52. Mollavali, M.; Falamaki, C.; Rohani, S. High performance NiS-nanoparticles sensitized TiO_2 nanotube arrays for water reduction. *Int. J. Hydrog. Energy* **2016**, *41*, 5887–5901. [CrossRef]
53. Feng, M.; Liu, Y.; Zhang, S.-N.; Liu, Y.-P.; Luo, N.; Wang, D.-A. Carbon quantum dots (CQDs) modified TiO_2 nanorods photoelectrode for enhanced photocathodic protection of Q235 carbon steel. *Corros. Sci.* **2020**, *176*, 108919. [CrossRef]
54. Liu, Y.; Yu, C.-Y.; Dai, W.; Gao, X.H.; Qian, H.-S.; Hu, Y.; Hu, X. One-pot solvothermal synthesis of multi-shelled α-Fe_2O_3 hollow spheres with enhanced visible-light photocatalytic activity. *J. Alloys Compd.* **2013**, *551*, 440–443. [CrossRef]
55. Wan, N.; Xing, Z.-P.; Kuang, J.-Y.; Li, Z.-Z.; Yin, J.-W.; Zhu, Q.; Zhou, W. Oxygen vacancy-mediated efficient electron-hole separation for C-N-S-tridoped single crystal black TiO_2(B) nanorods as visible-light-driven photocatalysts. *Appl. Surf. Sci.* **2018**, *457*, 287–294. [CrossRef]
56. Eskizeybek, V.; Sarı, F.; Gülce, H.; Gülce, A.; Avcı, A. Preparation of the new polyaniline/ZnO nanocomposite and its photocatalytic activity for degradation of methylene blue and malachite green dyes under UV and natural sun lights irradiations. *Appl. Catal. B Environ.* **2012**, *119–120*, 197–206. [CrossRef]
57. Li, Y.-J.; George, P. Demopoulos; Precipitation of nanosized titanium dioxide from aqueous titanium(IV) chloride solutions by neutralization with MgO. *Hydrometallurgy* **2008**, *90*, 26–33. [CrossRef]
58. Dimitrakopoulou, D.; Rethemiotaki, I.; Frontistis, Z.; Xekoukoulotakis, N.P.; Venieri, D.; Mantzavinos, D. Degradation, mineralization and antibiotic inactivation of amoxicillin by UV-A/TiO_2 photocatalysis. *J. Environ. Manag.* **2012**, *98*, 168–174. [CrossRef]
59. Murgolo, S.; Petronella, F.; Ciannarella, R.; Comparelli, R.; Agostiano, A.; Curri, M.L.; Mascolo, G. UV and solar-based photocatalytic degradation of organic pollutants by nano-sized TiO_2 grown on carbon nanotubes. *Catal. Today* **2015**, *240*, 114–124. [CrossRef]
60. Mohite, S.V.; Kim, S.; Lee, C.; Bae, J.; Kim, Y. Z-scheme heterojunction photocatalyst: Deep eutectic solvents-assisted synthesis of Cu_2O nanocluster improved hydrogen production of TiO_2. *J. Alloys Compd.* **2022**, *928*, 167168. [CrossRef]
61. Chen, Y.; Li, H.; Wang, Z.-P.; Tao, T.; Hu, C. Photoproducts of tetracycline and oxytetracycline involving self-sensitized oxidation in aqueous solutions:effects of Ca_2^+ and Mg^{2+}. *J. Environ. Sci.* **2011**, *23*, 1634–1639. [CrossRef]
62. Ahmadi, M.; Motlagh, H.R.; Jaafarzadeh, N.; Mostoufi, A.; Saeedi, R.; Barzegar, G.; Jorfi, S. Enhanced photocatalytic degradation of tetracycline and real pharmaceutical wastewater using MWC NT/TiO_2, nano-composite. *J. Environ. Manag.* **2017**, *186*, 55–63. [CrossRef] [PubMed]

63. Wan, J.; Xue, P.; Wang, R.-M.; Liu, L.; Liu, E.-Z.; Sai, X.; Fan, J.; Hu, X.-Y. Synergistic effects in simultaneous photocatalytic removal of Cr(VI) and tetracycline hydrochloride by Z-scheme $Co_3O_4/Ag/Bi_2WO_6$ heterojunction. *Appl. Surf. Sci.* **2019**, *483*, 677–687. [CrossRef]
64. Xu, Q.-L.; Zhang, L.-Y.; Yu, J.-Q.; Swelm, W.; Al-Ghamdi, A.A.; Jaroniec, M. Direct Z-scheme photocatalysts: Principles, synthesis, and applications. *Mater. Today* **2018**, *21*, 1042–1063. [CrossRef]
65. Wang, J.; Wang, G.-H.; Wang, X.; Wu, Y.; Su, Y.; Tang, H. 3D/2D direct Z-scheme heterojunctions of hierarchical TiO_2 microflowers/g-C_3N_4 nanosheets with enhanced charge carrier separation for photocatalytic H_2 evolution. *Carbon* **2019**, *149*, 618–626. [CrossRef]